ACS OMEGA

http://pubs.acs.org/journal/acsodf

Article

Biodegradable Protein-Stabilized Inorganic Nanoassemblies for Photothermal Radiotherapy of Hepatoma Cells

Pranjali Yadav, Shubhra Chaturvedi, Samir Kumar Biswas, Rohit Srivastava, Kamalakannan Kailasam,* Anil Kumar Mishra,* and Asifkhan Shanavas*

Cite This: *ACS Omega* 2022, 7, 8928–8937

Read Online

ACCESS | Metrics & More | Article Recommendations | Supporting Information

ABSTRACT: Inorganic nanomaterials require optimal engineering to retain their functionality yet can also biodegrade within physiological conditions to avoid chronic accumulation in their native form. In this work, we have developed gelatin-stabilized iron oxide nanoclusters having a primary crystallite size of ∼10 nm and surface-functionalized with indocyanine green (ICG)-bound albumin-stabilized gold nanoclusters (Prot-IONs). The Prot-IONs are designed to undergo disintegration in an acidic microenvironment of tumor in the presence of proteolytic enzymes within 72 h. These nanoassemblies demonstrate bio- and hemocompatibility and show significant photothermal efficiency due to strong near infrared absorption contributed by ICG. The surface gold nanoclusters could efficiently sensitize hepatoma cells to γ-irradiation with substantial cytoskeletal and nuclear damage. Sequential irradiation of Prot-ION-treated cancer cells with near infrared (NIR) laser (λ = 750 nm) and γ-irradiation could cause ∼90% cell death compared to single treatment groups at a lower dose of nanoparticles. The superparamagnetic nature of Prot-IONs imparted significant relaxivity (∼225 mM^{-1} s^{-1}) for T_2-weighted magnetic resonance imaging. Additionally, they could also be engaged as photoacoustic and NIR imaging contrast agents. This work demonstrates bioeliminable inorganic nanoassemblies with significant theranostic potential.

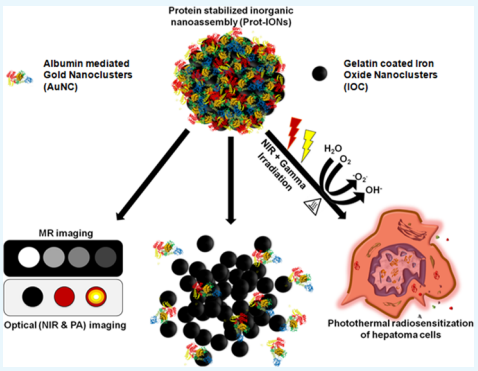

INTRODUCTION

Inorganic nanoparticles (INPs) have shown great potential in biomedical applications as drug delivery systems, imaging contrast agents, photothermal conversion agents due to their unique physicochemical characteristics, and so forth.[1−10] NP size, shape, and surface chemistry play an important role in the biodistribution, clearance, and *in vivo* toxicity. Modifying these physicochemical parameters would decide the fate of non-degradable INPs inside the body, as they are more stable compared to their organic counterparts.[11] Long-term accumulation of these INPs in the body may induce several irreversible changes in the body due to oxidative stress and impairment in the mononuclear phagocytic system.[12] Hence, bioelimination of INPs is essential for the clinical translation to prohibit any chronic toxicity risks.

Gold-based INPs have been widely used for photothermal cancer therapy and cancer theranostics.[13−15] Gold NPs having sizes larger than 50 nm have better accumulation in the tumor tissues due to the electron paramagnetic resonance effect, but they could not be excreted from the glomerulus filtration. For instance, the intravenous injection of PEGylated hollow gold nanospheres having size 50 nm had an excretion of only ∼4% of the injected dose within 1 month. The proteomic profiling of liver depicted an irreversible change in the liver after 3 months.[16] In another study, PEGylated gold nanoshells decorated on silica NPs of size ∼150 nm injected intravenously in Beagle dogs showed no chronic toxicity over a period of 10 months but with considerable accumulation in the liver and spleen.[17] All these studies indicate that to overcome long-term side effects, INPs should be sized less than 6 nm for rapid clearance via the renal route. However, at this ultrasmall size regime, a standalone isotropic structure has limited room for tuning application-oriented functional properties.

Metal nanoclusters having ultrasmall size with a core size between 0.5 and 3 nm, and versatile photoluminescent properties have gained attention in the biomedical field in the past decade.[18−23] Gold nanoclusters have been shown to undergo renal clearance, especially depending upon the ligand type and density.[24,25] Considering their unique optical and radiosensitization properties, their potential in cancer therapy is constantly being explored.[26,27] Glutathione-stabilized AuNC conjugated with Indocyanine green (ICG) served as an effective near infrared (NIR) light-responsive photothermal

Received: December 28, 2021
Accepted: February 17, 2022
Published: March 4, 2022

agents. This study showcases the complete tumor ablation followed by bioelimination of these AuNCs from the body.[28] In another study by Zhang et al., GSH- and bovine serum albumin (BSA)-capped AuNCs were evaluated for cancer radiation therapy. GSH-capped AuNCs demonstrate a significant decrease in the tumor volume as compared to the radiation-alone group.[29]

Gelatin is a polypeptide obtained from denatured collagen, which exhibits excellent biocompatibility and nonimmunogenicity. It has been approved by USFDA for extravascular administration and has been used for numerous biomedical applications.[30−32] Gelatin can easily disintegrate inside the body by matrix metallo proteinases (MMPs) expressed in many tissues. MMPs are a family of proteases that are upregulated in tumor tissues and have been extensively studied as a cancer biomarker.[33] For instance, size-controllable supramolecular gelatin NPs decorated with quantum dot (QD) payload have been utilized for cancer cell imaging. These NPs disassemble in the presence of MMPs and release QDs toward tumor detection.[34] In another study, doxorubicin and dendritic poly-L-lysine were fabricated on gelatin NPs that could be degraded by MMP-2 to smaller size NPs, improving the tumor penetration and therapeutic efficiency *in vivo*.[30]

Considering size requirements for *in vivo* utilization, a multifunctional protein-stabilized inorganic nanoassembly (Prot-ION) has been synthesized. The Prot-IONs consist of a core made of gelatin-stabilized iron oxide nanoassemblies (IONs) having a primary crystallite size of ∼10 nm and an albumin-stabilized AuNC shell. The gelatin-based core is enriched with numerous amino acids that offer sites for adsorption of albumin-based AuNCs without additional surface modification. The AuNCs were also bound with ICG dye for incorporating optical imaging and photothermal transduction functionalities due to its strong NIR absorption. The rationale to use proteins, gelatin and albumin, as a stabilizer for both IONs and AuNCs, respectively, is to have the ability to degrade in the local microenvironment of the tumor with acidic pH and enzymes, collapsing into small particles that qualify for effective renal and hepatobiliary clearance from the body.

MATERIALS AND METHODS

Materials Used. Iron(III) chloride hexahydrate ($FeCl_3 \cdot 6H_2O$), chloroauric acid trihydrate, *N*,*N*′-diethyl-*p*-phenylenediamine (DPD), BSA, and ICG (Cardiogeen) were purchased from Sigma-Aldrich. Ethylene glycol (EG) and sodium acetate (NaAc) were obtained from TCI Chemicals. Gelatine powder 240 Bloom (Bacto) was procured from S.D. Fine-chem limited. Double distilled water was used for all synthetic experiments. All the chemicals were of analytical grade and used as received. MTT, bisbenzimide (Hoechst 33342), and phalloidin-TRITC conjugate were purchased from Sigma-Aldrich. PLC/PRF/5 cell lines were purchased from the National Center of Cell Science (NCCS, Pune, India). Human umbilical vein endothelial cells (HUVECs) was purchased from Lonza (Cat. no. 2517A) and maintained in endothelial growth medium from Lonza (Cat. no. 3162). Dulbecco's modified Eagle medium (DMEM, HiMedia) was used in supplementation with 10% fetal bovine serum (FBS, HiMedia) and 1% antibiotic/antimycotic solution (HiMedia). Proteinase K was purchased from Ambion RNA by Life Technologies.

Synthesis of Iron Oxide Nanocluster. Gelatin-coated iron oxide nanoclusters (IOCs) were synthesized according to a previous report with some modification.[35] Gelatin (300 mg) was dissolved in 20 mL of EG at 80 °C until it formed a transparent solution. Next, $FeCl_3 \cdot 6H_2O$ (1.2 mmol) was added to the mixture to form a clear solution, followed by the addition of NaAc (900 mg). The mixture was stirred vigorously for 60 min and sealed in a Teflon-lined stainless steel autoclave. The reaction was kept at 200 °C for 6 h and allowed to cool to room temperature (RT). A dark brown colored product was obtained by centrifugation. The product was washed three times with water by magnetic separation and finally dispersed in water at a concentration of 10 mg/mL and stored at 4 °C.

Synthesis of AuNCs. BSA-mediated gold nanoclusters (AuNCs) were synthesized by a previously reported method with some modifications. 5 mL aqueous solution of $HAuCl_4$ solution (10 mM) was added to 5 mL of BSA solution (50 mg/mL) under vigorous stirring. After 10 min, 1 M NaOH solution was added into the solution and kept under stirring at 60 °C for 6 h until the color of the solution changed from light yellow to deep brown. The synthesis was carried out under dark conditions.

Preparation of Prot-IONs. The preparation of Prot-IONs (protein stabilized inorganic nanoassemblies) was done in two parts. First, to optimize the coating of AuNCs on IOC, a fixed concentration of 1 mL IOC (0.5 mg/mL) was incubated with different volumes of AuNCs. The samples were incubated overnight at 180 rpm at 37 °C in an incubator. Next day, the samples were washed magnetically two times with water and redispersed in water. The fluorescence spectra of all the redispersed samples were recorded. In the second part, ICG was loaded onto AuNCs by the noncovalent binding process. AuNC−ICG was prepared by the addition of 2 mL ICG solution (2 mg/mL) to 1 mL AuNC under vigorous magnetic stirring at RT for 1 h. After that, to remove the excess ICG, the solution was dialyzed by ultrapure water using a dialysis membrane (7000 MW) for 3 h. The as-synthesized AuNC−ICG was stored at 4 °C with light proof package.

AuNC−ICG suspension (3 mL) was incubated with 0.5 mg/mL IOC and kept for shaking overnight at RT. Next day, the samples were washed two times with deionized water magnetically to remove unbound AuNC−ICG particles. The pellet was redispersed in water and stored at 4 °C under dark conditions until further use.

Characterization. The structural morphology, size, and shape of IOC and Prot-ION were visualized using the transmission electron microscope (JEOL JEM-2100) at an accelerating voltage of 200 kV. The transmission electron microscopy (TEM) samples were drop-cast on a 400 mesh copper grid coated with a perforated carbon film after dispersing them in water. A Cary series UV−Vis−NIR spectrophotometer (Agilent Technologies) was used to optimize the coating of AuNC−ICG on IOC using a quartz cuvette (1 cm path length). Photoluminescence spectra were recorded at RT using a FS5 steady state fluorescence spectrometer (Edinburg instruments). A Zetasizer Nano ZSP (Malvern) instrument was used for the surface charge measurements. To determine the elemental composition and oxidation states of Au, Fe, and O, X-ray photoelectron spectroscopy (XPS) was carried out using an ESCALAB 250xi Thermo scientific spectrometer using monochromatic Al Kα radiation (1486.6 eV).The magnetic properties were measured using a vibrating sample magnetometer (model 7410, Lake Shore) at 300 K.

https://doi.org/10.1021/acsomega.1c07324
ACS Omega 2022, 7, 8928−8937

Hydroxyl Ion (•OH) Generation by Fenton Reaction. *N*,*N*′-diethyl-p-phenylene diamine (DPD) was employed as a detecting probe to examine the •OH ion generation by the Fenton mechanism. 100 μg/mL Prot-ION and 10 mM DPD were mixed in a solution containing 100 μM H_2O_2 under the acidic condition (pH 5.2). The •OH ion generation was monitored up to 60 min by recording the absorbance spectra from 400−700 nm at regular intervals of 10 min. The same set of experiments repeated in the absence of Prot-ION served as the control.[36]

Biodegradation Studies. Prot-IONs were incubated with acetate buffer (pH = 5.2) to mimic the tumor microenvironment. Proteinase-K (10 μg/mL) was introduced to stimulate the enzyme-containing microenvironment. The samples were incubated up to 3 days at 37 °C under uniform shaking conditions (150 rpm/min).The particles were observed under TEM at different time intervals to observe the biodegradation of Prot-IONs.[37]

Photothermal Transduction Experiments. Photothermal transduction studies were performed using a 750 nm near-infrared laser (Shanghai MR Trade International Co. Ltd) with a maximum power output of 650 mW. Prot-ION was well dispersed in water at a concentration of 500 μg/mL and illuminated with the laser for 4 min. The heating and cooling cycles were carried out to record the temperature using the FLIR One pro thermal imager.

***In Vitro* Biocompatibility.** The biocompatibility of Prot-ION was evaluated against HuVEC cells using an MTT assay. Briefly, 200 μL of cells was seeded in a 96-well flat culture plate at a density of 2.5×10^4 cells per well and cultured for 24 h at 37 °C and 5% CO_2. The cells were incubated with varying concentrations of Prot-ION for 48 h. Subsequently, the cells were washed with prewarmed 1× PBS thrice to remove traces of the sample. 20 μL of MTT solutions (5 mg/mL in PBS) diluted with 180 μL media was added to the wells and incubated for 4 h. After 4 h, the plates were centrifuged at 1500 rpm for 5 min at RT. 150 μL of dimethyl sulfoxide was added to each well to dissolve the formazan crystals, and all the wells were aspirated well before taking absorbance. The absorbance of the suspension was measured at 570 nm on an ELISA reader. Cell viability was calculated by the following formula

$$\text{Cell viability}(\%) = \frac{\text{absorbance of the treated cells}}{\text{absorbance of the control cells}} \times 100$$

Hemolysis Assay. The blood compatibility of Prot-ION was studied by Harboe's method. With ethical approval from IIT Bombay institute ethics committee (IITB-IEC/2019/031), 5 mL of blood was withdrawn from healthy volunteers and collected in trisodium citrate-coated tubes. Different concentrations of Prot-ION resuspended in 0.9% saline were incubated with blood for 3 h at 37 °C under mild shaking conditions. 0.9% saline and 1% Triton X100 served as negative and positive controls, respectively. The treated blood was centrifuged at 4500 rpm for 10 min, and the absorbance for collected plasma was recorded at 380, 415, and 450 nm. The amount of hemoglobin was calculated by the following formula

$$\text{Amount of plasma hemoglobin}\left(\frac{mg}{dL}\right) = 0.076[2(A_{415}) - (A_{380} + A_{450})] \times \text{D. f.}$$

where A_{380}, A_{415}, and A_{450} are the absorbance values at 380, 415, and 450 nm, respectively. D.f. is the dilution factor used for taking the absorbance. The percentage of hemolysis was calculated by the following equation

$$\%\ \text{hemolysis} = \frac{\text{plasmaHb}_{\text{test}}}{\text{plasmaHb}_{\text{blood}}} \times 100$$

where plasma Hb_{test} and plasma Hb_{blood} correspond to the plasma hemoglobin value of test samples and the whole blood, respectively.

Localization of Prot-ION in PLC/PRF/5 Cells. For the intracellular localization of Prot-ION, the cells were seeded on a coverslip and allowed to grow overnight. Next day, the cells were treated with Prot-ION for 6 h and fixed with 4% PFA. After fixation, the nuclei and cytoskeleton were stained using Hoechst 33342 and Ph-TRITC, respectively. The cells were mounted on a glass slide and taken for imaging under a LSM 880 confocal microscope.

***In Vitro* Photothermal Therapy.** The *in vitro* cytotoxicity of different concentrations of Prot-ION was assessed on PLC/PRF/5 cells, using the MTT assay. Specifically, 200 μL of cells was seeded in a 96-well flat culture plate at a density of 5×10^3 cells per well and incubated for 24 h at 37 °C under 5% CO_2. After overnight incubation, samples with different concentrations (all the dilutions were made in media) were added to each group. After 6 h incubation at 37 °C and 5% CO_2, the cells were exposed to 750 nm (650 mW) laser for 4 min. The plates were further incubated for 24 h at 37 °C and 5% CO_2. The cell viability was measured using the MTT assay.

***In Vitro* Radiation Therapy.** Cell viability of PLC/PRL/5 cells was tested against Prot-ION and AuNC−ICG with and without exposure to radiation doses (5 Gy). Briefly, 1×10^4 cells were seeded in a 96 well plate and allowed to grow overnight. Next day, the cells were treated with different concentrations (i.e. 62.5, 125, 250, and 500 μg/mL) of Prot-ION, BSA-AuNC, and Au NCs−ICG, respectively. After 24 h, the NP-treated cells were exposed to different radiation doses of 0, 1.25, 2.5, and 5 Gy followed by MTT assay.

Reactive Oxygen Species Assay. Reactive oxygen species (ROS) levels were measured by reaction with 2,7-dichlorofluorescein diacetate (DCFDA). DCFDA is a nonfluorescent dye, which can readily diffuse into the cells and is cleaved by intracellular esterases to form DCF by reaction with the ROS generated in cells. The quantity of ROS generated is directly proportional to green fluorescence emitted by DCF. Following radiation treatment, the ROS levels in media were determined by incubating cells with 500 μg/mL Prot-IONs, followed by exposure to radiation (5 Gy). The cells were washed with Hank's buffer and incubated with DCFDA (25 μg/mL in serum free media). The fluorescence intensity was recorded at 0 and 240 min (exc: 485 nm and em: 535 nm) and plotted with respect to control.

Cellular Damage Analysis. PLC/PRF/5 cells were seeded in a 6 well plate on cover slips with a density of 5×10^4 cells/well in DMEM supplemented with 5% FBS and were allowed to adhere for 24 h. The cells were incubated with Prot-ION for 24 h. The treated cells were then irradiated with a radiation dose of 5 Gy, washed three times with PBS, and fixed using 4% paraformaldehyde for 15−20 min at RT. Following incubation, they were irradiated with 5 Gy of γ-rays, washed twice in PBS, fixed with 4% paraformaldehyde. Fixed cells were stained with Hoechst (2 μg/mL) for 15 min, followed by counterstaining with Phalloidin-TRITC for 20 min. The cells were washed several times to remove any excess dye and

https://doi.org/10.1021/acsomega.1c07324
ACS Omega 2022, 7, 8928−8937

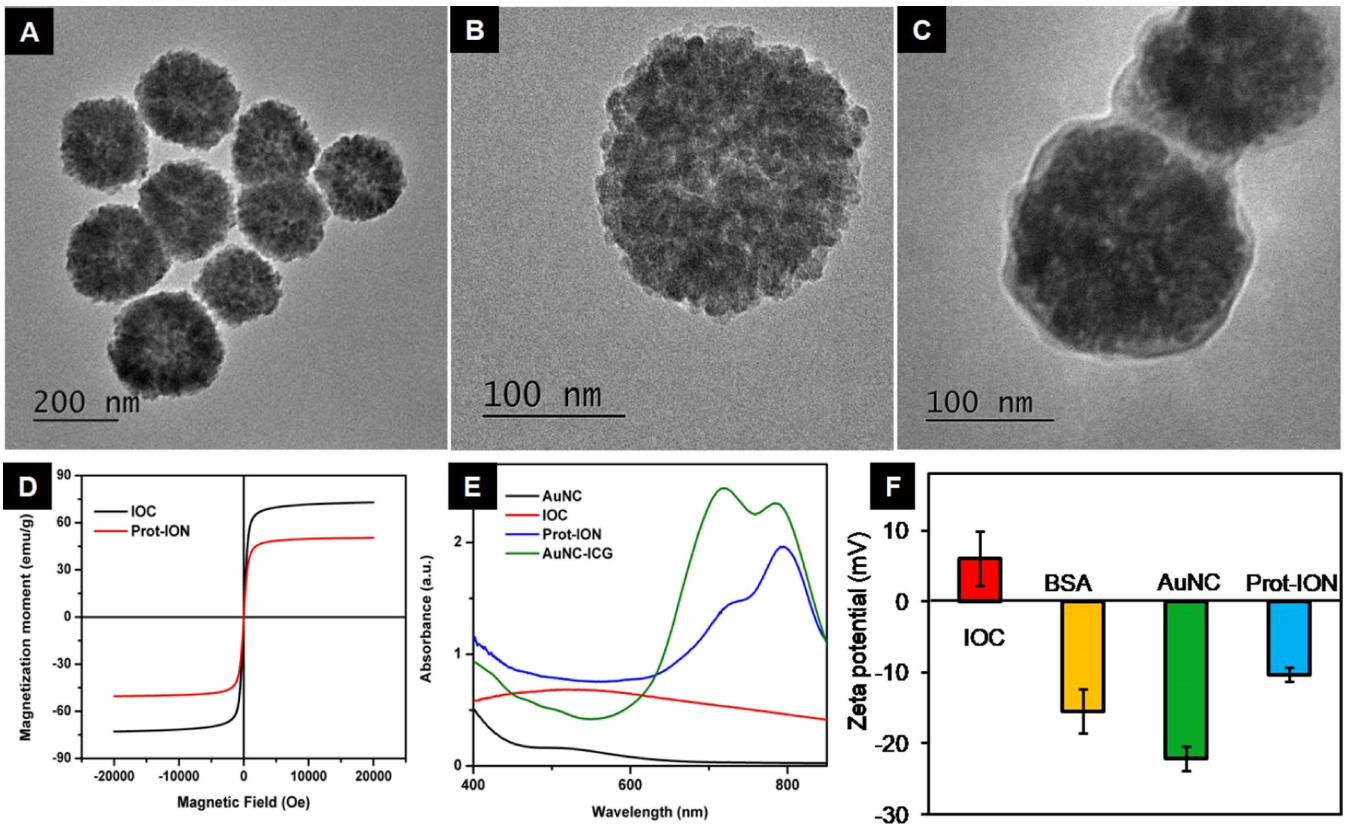

Figure 1. TEM image of (A,B) IOC and (C) Prot-ION; (D) magnetization moment and (E) visible−NIR spectra and (F) zeta potential of BSA, AuNC, IOC, and Prot-ION.

mounted with antifade mounting media as per manufacturer's protocol. The cellular and DNA damage was investigated using a confocal laser scanning microscope (Carl Zeiss LSM 880, Germany).

Photothermal Radiotherapy Study. To demonstrate the *in vitro* efficiency of combined photothermal therapy (PTT) and radiotherapy, PLC/PRL/5 cells were seeded at a density of 1×10^4 cells in a 96 well plate and allowed to attach overnight. The following day, cells were incubated with 250 μg/mL of Prot-ION and equivalent concentration of AuNC−ICG. After 6 h of incubation, the cells were exposed to a 750 nm laser for 4 min and placed back in the incubator for 18 h. Subsequently, the cells were exposed to a radiation of 5 Gy at a dose rate of 0.742 Gy/min. The MTT assay was performed to measure cell viability.

MR, Optical, and Photoacoustic Imaging. Phantom magnetic resonance (MR) images were acquired using a 7T BrukerBiospec MRI scanner (BrukerBioSpin MRI GmbH, Germany). Different concentrations of Prot-ION containing 1.5% agar gel were prepared in MilliQ water (in 1.5 mL micro centrifuge tubes). Images for quantifying $T2$ relaxation time were acquired using the rapid acquisition with the relaxation enhancement pulse sequence. Parameters for $T2$ quantification were effective echo time TE = 8, 24, 40, 56, 72, 88, 104, and 120 ms and repetition time TR = 5500 ms. Slice thickness and field of view for all acquisition were 1 mm and 6 × 4 cm, respectively. Origin 8.6 software was used to calculate the $T2$ values for each sample by exponential decay curve fitting. The r_2 relaxivities were calculated as the proportionality constants of the linear relation between the reciprocal relaxation time versus Fe concentration. For optical imaging, a three-dimensional imaging system was used to acquire the fluorescent images.

Different concentrations of Prot-ION were prepared in a 1% solidified agarose gel and loaded in 0.1 mm capillary voids for photoacoustic (PA) imaging. Pulsed array-light-emitting diode (LED) light (energy of each array LED = 200 μJ per pulse) was used to generate photoacoustic signals from samples. Two units of the array-LED-based pulsed excitation laser source (λ = 850 nm) were placed on both sides of a linear array transducer and had a central frequency of 7 MHz with 80% bandwidth. The photoacoustic and ultrasound signals were acquired using a 128-element linear array-based ultrasound detector. A high-speed 128-channel data acquisition system having 14 bit resolution (PreXion Corporation, Japan) was used to acquire the signals where the sampling rates for the photoacoustic signal and ultrasound signal acquisition were 40 and 20 MSPS, respectively. The normal delay sum algorithm was used to reconstruct the images.

RESULTS AND DISCUSSION

Synthesis and Characterization of Prot-IONs. IOCs were synthesized in a one-step hydrothermal method according to a previously reported protocol.[32] They showed uniform size distribution and a spherical morphology with a diameter of ∼220 nm. The TEM images of Prot-ION show a thick and uniform coating of albumin-stabilized AuNCs on the surface of IOC (Figure 1A−C). IOCs possess a subtle broad scattering cross section from the visible to the infrared region. However, after the AuNC−ICG coating, Prot-ION possessed strong absorbance at 730 and 790 nm that substantiated the presence of ICG (Figure 1E). The positive zeta potential of

https://doi.org/10.1021/acsomega.1c07324
ACS Omega 2022, 7, 8928−8937

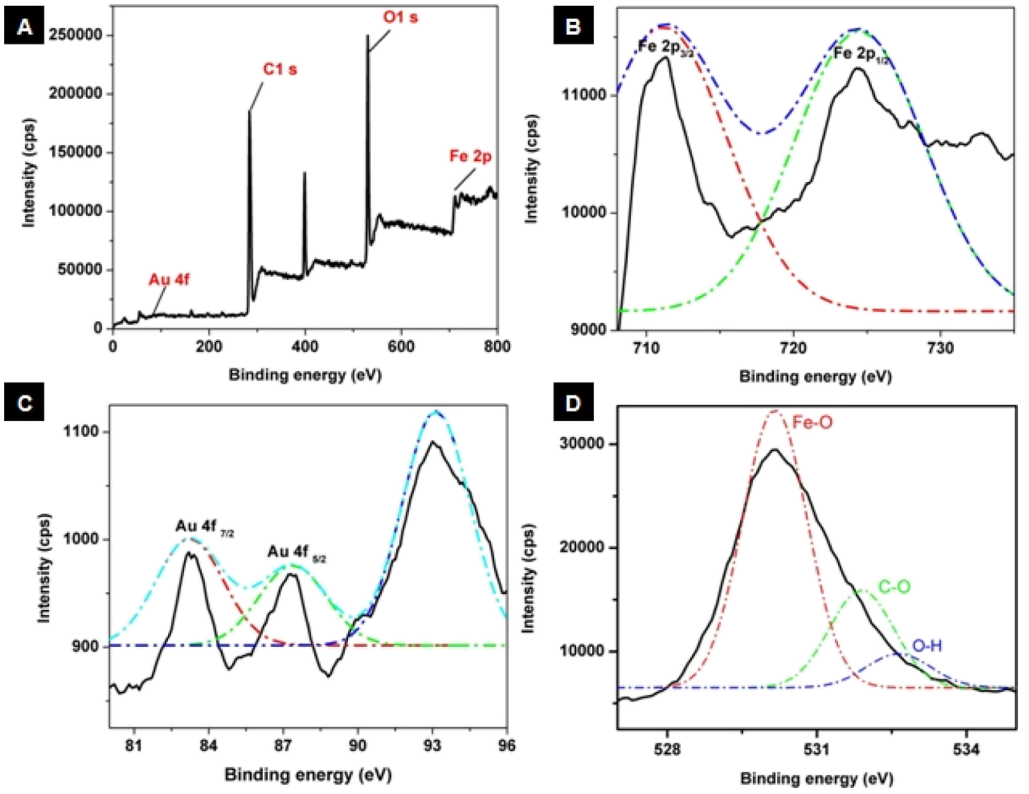

Figure 2. (A) XPS spectrum of Prot-ION, showing high-resolution plots corresponding to (B) Fe 2p, (C) Au 4f, and (D) O 1s.

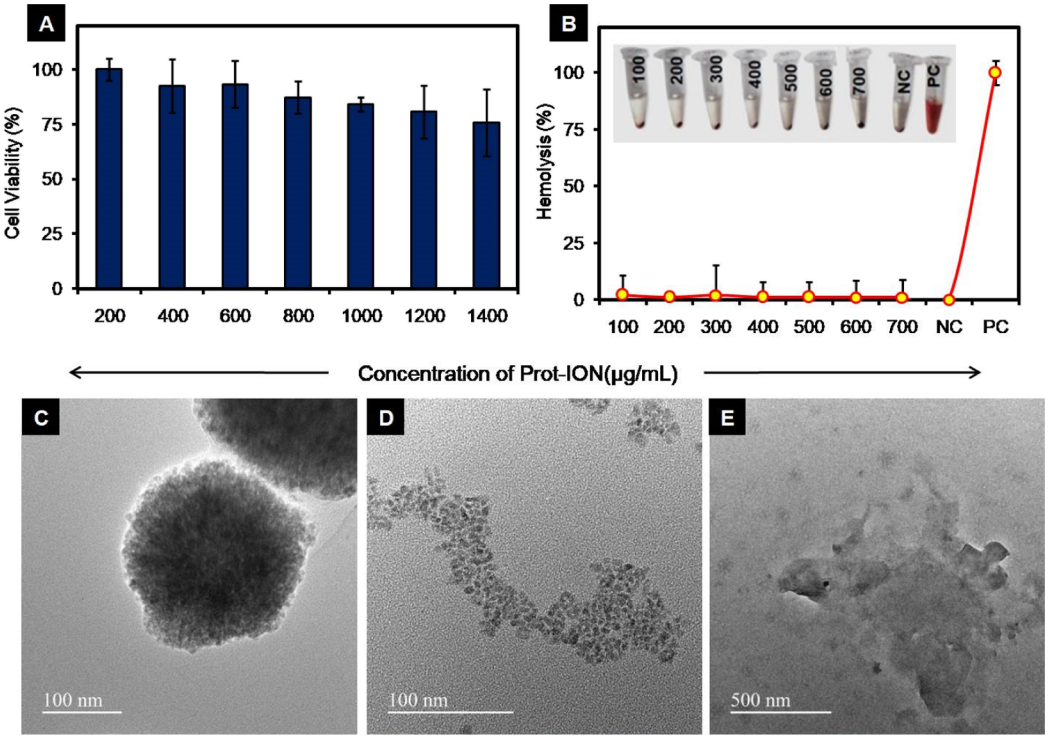

Figure 3. (A) Biocompatibility against HUVEC and (B) hemocompatibility of Prot-ION. TEM images revealing degradation of Prot-ION in the presence of proteinase K and acidic pH-5.2 after (C) 24, (D) 48, and (E) 72 h.

IOC (~6 mV) facilitated coating of AuNC−ICG via electrostatic adsorption, changing the overall zeta potential of Prot-ION to −10.3 mV (Figure 1F). The magnetization moments of IOC and Prot-ION were 72 and 49 emu/g, respectively, confirming superparamagnetic behavior (Figure 1D). The observed decrease in magnetization of Prot-ION is due to the presence of the albumin layer on their surface.

XPS was used to elucidate the elemental composition and oxidation states of all the elements present within Prot-IONs. A wide-range XPS spectrum indicated the presence of Au 4f, C

https://doi.org/10.1021/acsomega.1c07324
ACS Omega 2022, 7, 8928−8937

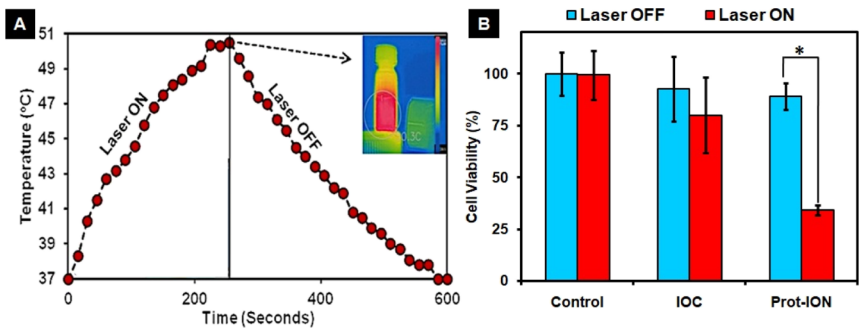

Figure 4. (A) Concentration-dependent photothermal response of Prot-IONs and (B) *in vitro* photothermal response of IOC and Prot-ION against PLC/PRF/5 with 5 min of laser treatment (*$P < 0.05$).

1s, O 1s, and Fe 2p, as shown in Figure 2. The deconvoluted peaks of Fe 2p spectra show binding energies corresponding to $2p_{3/2}$ and $2p_{1/2}$ at 710 and 724 eV, respectively. The spectra also point out two spin−orbit doublets that are characteristic of Fe^{2+} and Fe^{3+}. The O 1s spectrum could be deconvoluted into three peaks where 528.61 eV is a signature peak of Fe−O species, confirming the formation of Fe_3O_4, while the other two peaks could be attributed to the presence of residual groups such as C−O and O−H. The abovementioned results are in coherence with the reported values of Fe_3O_4. The Au 4f narrow spectrum with the characteristic doublet peak of Au $4f_{7/2}$ and Au $4f_{5/2}$ centered at 83.28 and 87.29 eV was observed, satisfying the separation of the Au 4f level of 3.6 eV. However, an additional peak was observed at 92.26 eV, which may be attributed to the presence of gold in the ground state.[38,39]

Biocompatibility, Hemocompatibility, and Biodegradation Studies. The biocompatibility of Prot-ION was determined against endotoxin-sensitive human umbilical cord vein endothelial cells. More than 85% cells remained viable up to a concentration of 1 mg/mL without showing any significant reduction (Figure 3A). As inferred from the bright-field images of cells, Prot-ION NPs showed concentration-dependent cytoplasmic localization within the cells (Figure S3). Hemocompatibility plays a critical role for assessing safety aspects of a nanomaterial. Prot-IONs did not inflict any hemoglobin leakage from RBCs for up to a concentration of 700 μg/mL[40] (Figure 3B). On the contrary, the positive control (1% Triton X-100) caused complete hemolysis of RBCs, showing a high amount of hemoglobin release in the supernatant. The abovementioned results confirm the nontoxic, biocompatible, and hemocompatible nature of Prot-IONs.

The biodegradability of Prot-ION was studied for 72 h in acidic buffer (5.2) in the presence of Proteinase-K to mimic intracellular and tumor microenvironment.[41] The structural disintegration of Prot-ION started in the first 24 h with the degradation of the outer protein layer consisting of the AuNCs, which was absent, as seen in Figure 3C. After 48 h, destabilization of the core IOC due to the action of proteinase-K on gelatine was evident from the loss of the three-dimensional structure and distribution of crystallites of size less than 10 nm on the same plane of the focus (Figure 3D). When the time of incubation was prolonged to 72 h, the IOCs had completely degraded with the complete absence of any remnants of the original nanostructure (Figure 3E). This confirms that low pH and presence of the enzymes could accelerate the breakdown of these nanoassemblies, confirming their ability to degrade in tumor microenvironment. The rate of degradation would depend upon the amount of hydroxyl ions and proteolytic enzymes present in both intracellular and extracellular compartments of the tumor. Previous reports have confirmed that Fe_3O_4 NPs can seamlessly disintegrate *in vivo* and Fe ion gets translocated through different pathways contributing to their critical role in iron homeostasis.[42]

***In Vitro* PTT.** Due to the presence of strong NIR absorption between 700 and 800 nm contributed by ICG, Prot-IONs could act as a photothermal transducer. While no obvious PLC/PRF/5 cell death was observed upon exposure to the 750 nm laser alone, photothermal killing was more pronounced in Prot-ION (500 μg/mL)-treated cells. The viability of PP5 cancer cells decreased drastically from ∼90 to ∼35% after the NIR light irradiation (Figure 4A,B).[43]

Radiotherapy and Fenton-Mediated Induction of Oxidative Stress with Prot-ION. High energy ionizing radiation stimulates the generation of ROS that potentially cause physical damages to macromolecular structures such as DNA, protein, and membrane lipids, eventually leading to cell death. These effects can be exponentiated with radiosensitizers such as AuNCs. Hypothesizing that Prot-Ion could expound the detrimental effects of radiotherapy, the PLC/PRF/5 hepatoma cells were treated with the nanoassemblies for 24 h, followed by exposure to 5 Gy γ-irradiation. Prot-IONs were localized in the cytoplasm of the cancer carcinoma cells with intact nuclei and cytoskeleton, corroborating its compatibility at 500 μg/mL (Figure 5A). As can be observed in Figure 5B(ii), the cells treated with radiation alone demonstrated trivial nuclear and cytoskeletal damage in comparison to the control. Treatment with Prot-ION ameliorated with a decrease in cell density with damage to the nuclear and cytoskeletal structures [Figure 5B(iii)]. These results affirm the radiosensitization effect of Prot-IONs against hepatoma cells.[44−46]

Excessive intracellular ROS in the cells could perturb the equilibrium of the oxidation reduction potential and lead to intracellular peroxide production followed by a series of adverse biological effects. ROS usually refers to superoxide anion ($^{\bullet}O_2^-$), hydrogen peroxide (H_2O_2), hydroxyl radical ($^{\bullet}OH$), and singlet oxygen ($^1O_2$). *In vitro* ROS generation following γ-irradiation was assessed using DCF-DA as an intracellular probe. Radiation dose of 5 Gy over cells treated with IOC or AuNC−ICG showed an increase in the probe fluorescence, which is attributed to the production of ROS. However, Prot-ION-treated cells showed a twofold increase in fluorescence within 4 h of γ-irradiation (Figure 6C). As a consequence, there was a significant decrease in the viability (∼80%) of hepatoma cells treated with Prot-ION and exposed

https://doi.org/10.1021/acsomega.1c07324
ACS Omega 2022, 7, 8928−8937

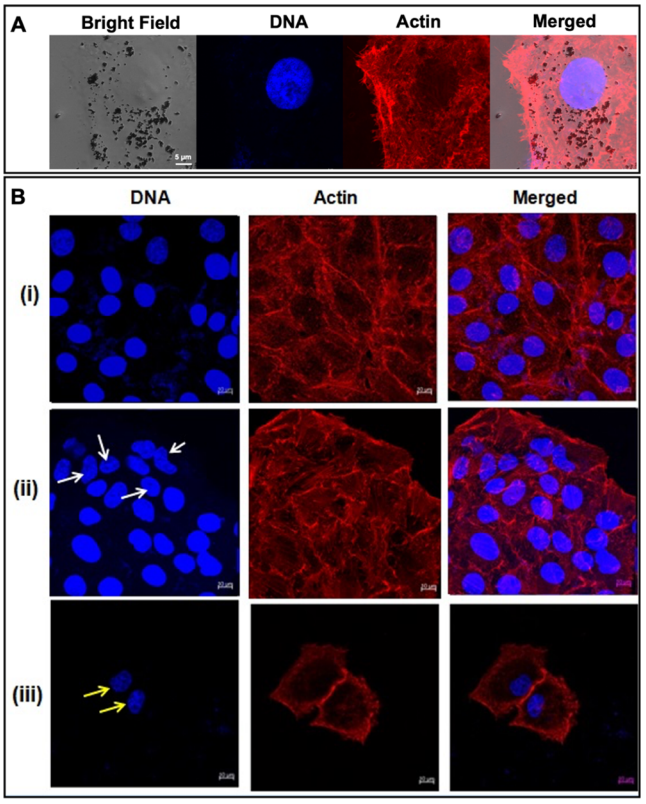

Figure 5. Confocal images of (A) nonirradiated PP5 cells with Prot-IONs localized around the nucleus and (B) confocal images of (i) untreated control, (ii) radiation-treated, and (iii) Prot-ION (500 μg/mL) + radiation (5 Gy)-treated PP5 cells stained with Hoechst (DNA) and phalloidin−TRITC (Actin).

to 5 Gy radiation as compared to equivalent concentration of IOC or AuNC−ICG.

After the intracellular uptake of Prot-ION, in the lysosomal acidic pH 5.2, the IOCs are converted to Fe^{+2}/Fe^{+3} ions.[47,48] Ferrous/ferric ions persuade the generation of free hydroxyl species due to the Fenton reaction, which was investigated by using DPD as a sensor molecule. As shown in Figure S4, there was a 10-fold increase in the amount of $^{\bullet}OH$ ions within 20 min at pH 5.2. These results substantiate the potential of Prot-IONs to activate the production of hydroxyl ions by Fenton reaction. Pronounced oxidative stress could be induced through Fenton reaction and mediated synergistically augmented ROS generation.

Combined Photothermal Radiotherapy with Prot-IONs. As radiosensitization with Prot-ION caused more than 50% cancer cell death at a concentration of 250 μg/mL (Figure 6B), sequential NIR laser exposure for 4 min and different radiation doses (0.625 to 5 Gy) at this concentration yielded up to ∼30% more cell death compared to cells exposed to radiation alone (Figure 6D).[49,50]

MR and Optical (NIR and Photoacoustic) Imaging. Furthermore, the ability of Prot-IONs to act as MR and optical contrast agents was evaluated. Figure 7A,C shows MR phantom images and the corresponding relaxivity (R_2) plot of Prot-IONs at a concentration range 0−0.08 mM of Fe. The R_2 value (∼225 mM^{-1} s^{-1}) of Prot-ION is significantly high compared to a commercial iron oxide-based contrast agent (85 mM^{-1} s^{-1}).[51,52] NIR optical images showed a concentration-dependent increase in fluorescence from Prot-IONs. As shown in Figure 7A,B, Prot-IONs also demonstrated concentration-dependent enhanced photoacoustic contrast in a simulated microvessel of 100 μm diameter.[53,54] These results indicate that Prot-IONs can serve as a versatile imaging contrast agent.

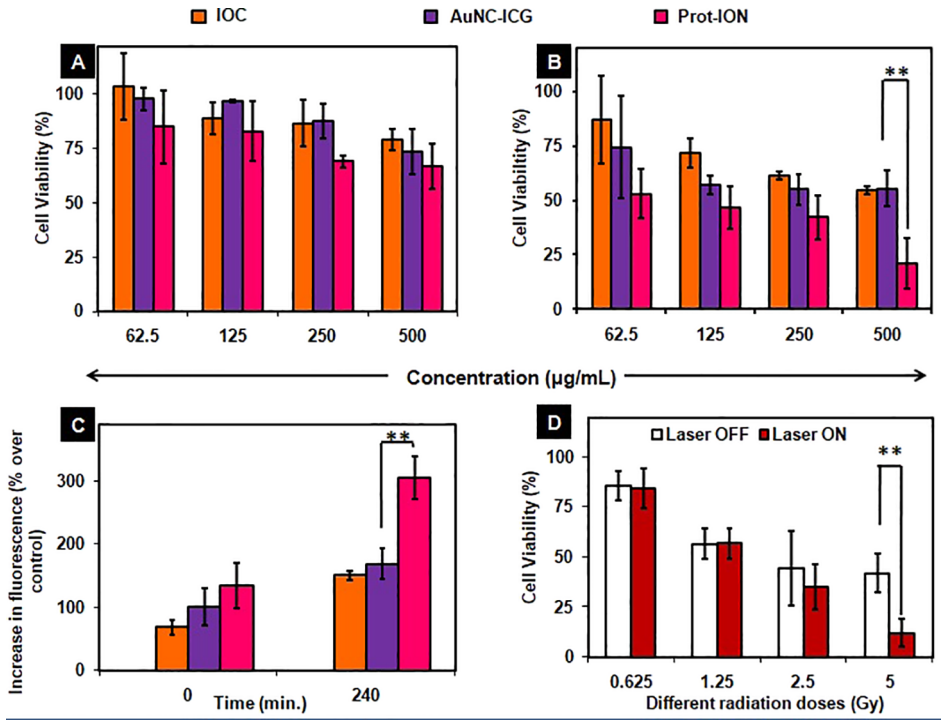

Figure 6. Percentage of viable cells treated with different concentrations of IOC, AuNC−ICG, and Prot-ION in the (A) absence and (B) presence of 5 Gy irradiation. (C) Intracellular ROS percentage recorded at two different time intervals. (D) Combinatorial effect of PTT and RT on PP5 cells treated with different radiation doses (**$P \leq 0.0065$).

https://doi.org/10.1021/acsomega.1c07324
ACS Omega 2022, 7, 8928−8937

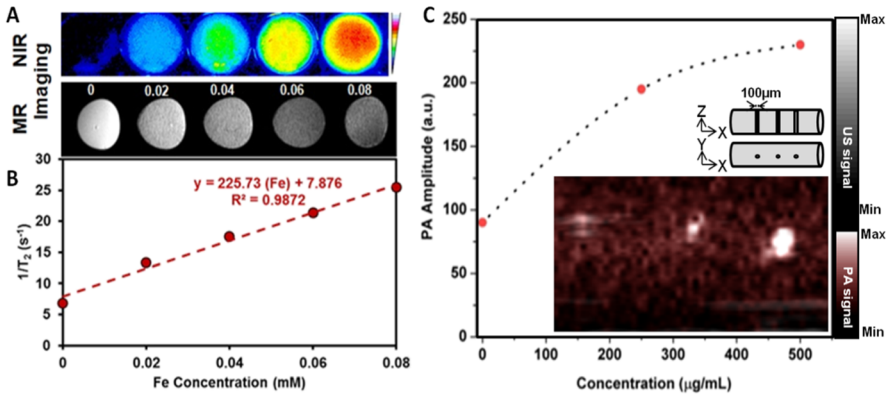

Figure 7. (A) Phantom T2-weighted MR images and optical images of varying concentrations of Prot-ION and (C) relaxivity plot of Prot-ION corresponding to varying iron concentrations; (B) phantom photoacoustic (PA) imaging of 100 μm wide capillary void inside 1% agarose.

CONCLUSIONS

Recently, there is significant interest in how to utilize nondegradable inorganic nanomaterials for biomedical applications and also clear them out of the body after their intended *in vivo* utilization. In this work, biodegradable magnetic and NIR active nanoassemblies functionalized with gold nanoclusters are showcased as potential theranostic agents. While they could sensitize cancer cells for photothermal radiation therapy and possess magnetic and optical properties for trimodal imaging (MRI, NIR, and PA) applications, they also collapsed into small NPs within 72 h in acidic pH and proteolytic conditions. Such engineered approaches to derive biodegradable inorganic nanomaterials would make them more suitable for *in vivo* applications.

ASSOCIATED CONTENT

Supporting Information

The Supporting Information is available free of charge at https://pubs.acs.org/doi/10.1021/acsomega.1c07324.

Dynamic light scattering, excitation/emission spectra, fluorescent images of AuNC, optimization of AuNC adsorption on IOCs, and field images of HuVEC cells incubated with different concentrations of Prot-ION (PDF)

AUTHOR INFORMATION

Corresponding Authors

Kamalakannan Kailasam − *Institute of Nano Science and Technology, SAS Nagar, Punjab 140306, India;* orcid.org/0000-0002-5931-7649; Email: kamal@inst.ac.in

Anil Kumar Mishra − *Division of Cyclotron and Radiopharmaceutical Sciences, Institute of Nuclear Medicine and Allied Sciences, DRDO, Delhi 110054, India;* orcid.org/0000-0003-2523-9045; Email: akmishra@inmas.drdo.in

Asifkhan Shanavas − *Institute of Nano Science and Technology, SAS Nagar, Punjab 140306, India;* orcid.org/0000-0001-7221-7477; Email: asifkhan@inst.ac.in

Authors

Pranjali Yadav − *Institute of Nano Science and Technology, SAS Nagar, Punjab 140306, India*

Shubhra Chaturvedi − *Division of Cyclotron and Radiopharmaceutical Sciences, Institute of Nuclear Medicine and Allied Sciences, DRDO, Delhi 110054, India;* orcid.org/0000-0003-0285-2111

Samir Kumar Biswas − *Department of Physical Sciences, Indian Institute of Science Education & Research Mohali, Manauli 140306, India*

Rohit Srivastava − *Department of Biosciences & Bioengineering, Indian Institute of Technology Bombay, Mumbai, Maharashtra 400076, India;* orcid.org/0000-0002-3937-5139

Complete contact information is available at: https://pubs.acs.org/10.1021/acsomega.1c07324

Notes

The authors declare no competing financial interest.

ACKNOWLEDGMENTS

P.Y. is thankful to the Institute of Nano Science and Technology for the Doctoral Fellowship. The study is supported by the Government of India under SERB core research grant scheme (EMR/2016/003851) and DST Nanomission scheme (SR/NM/NS-1108/2016). The authors are thankful to Dr. S.T. Nishanthi for helping us with the XPS studies at Electrochemical Power Sources Division, CSIR-Central Electrochemical Research Institute, Karaikudi—630003, Tamil Nadu, India. A.S. wishes to thank Prof. Manzoor Koyakutty, Amrita Center for Nanosciences and Molecular Medicine (ACNSMM) for his constant motivation and support.

REFERENCES

(1) Tang, F.; Li, L.; Chen, D. Mesoporous silica nanoparticles: synthesis, biocompatibility and drug delivery. *Adv. Mater.* **2012**, *24*, 1504−1534.

(2) Lima-Tenório, M. K.; Pineda, E. A.; Ahmad, N M.; Fessi, H.; Elaissari, A. Magnetic nanoparticles: In vivo cancer diagnosis and therapy. *Int. J. Pharm.* **2015**, *493*, 313.

(3) Liong, M.; Lu, J.; Kovochich, M.; Xia, T.; Ruehm, S. G.; Nel, A. E.; Tamanoi, F.; Zink, J. I. Multifunctional inorganic nanoparticles for imaging, targeting, and drug delivery. *ACS Nano* **2008**, *2*, 889−896.

(4) Cheng, L.; Wang, C.; Feng, L.; Yang, K.; Liu, Z. Functional nanomaterials for phototherapies of cancer. *Chem. Rev.* **2014**, *114*, 10869−10939.

(5) Lim, E.-K.; Kim, T.; Paik, S.; Haam, S.; Huh, Y.-M.; Lee, K. Nanomaterials for theranostics: recent advances and future challenges. *Chem. Rev.* **2015**, *115*, 327−394.

(6) Loynachan, C. N.; Soleimany, A. P.; Dudani, J. S.; Lin, Y.; Najer, A.; Bekdemir, A.; Chen, Q.; Bhatia, S. N.; Stevens, M. M. Renal clearable catalytic gold nanoclusters for in vivo disease monitoring. *Nat. Nanotechnol.* **2019**, *14*, 883−890.
(7) Houjuan, Z.; Zibiao, L.; Enyi, Y.; David, T.L. Oxygenic Enrichment in Hybrid Ruthenium Sulfide Nanoclusters for an Optimized Photothermal Effect. *ACS Appl. Mater. Interfaces* **2021**, *13*, 60351−60361.
(8) Yuhuan, L.; Huayuan, T.; Houjuan, Z.; Aleksandr, K.; Di, W.; Nicholas, A.; Yunxiang, S.; Aparna, N.; Eunbi, K.; Thomas, P.D.; David, T.L.; Feng, D.; Pu, C. K. *ACS Appl. Mater. Interfaces* **2021**, *13*, 29936−29948.
(9) Ding, X.; Peng, F.; Zhou, J.; Gong, W.; Slaven, G.; Loh, K. P.; Lim, C. T.; Leong, D. T. Defect engineered bioactive transition metals dichalcogenides quantum dots. *Nat. Commun.* **2019**, *10*, 41.
(10) Pranjali, Y.; Cheng, Z.; Andrew, K.W.; Kamalakannan, K.; Asifkhan, S. Magnetic and Photocatalytic Curcumin Bound Carbon Nitride Nanohybrids for Enhanced Glioma Cell Death. *ACS Biomater. Sci. Eng.* **2019**, *5*, 6590−6601.
(11) Zhu, M.; Nie, G.; Meng, H.; Xia, T.; Nel, A.; Zhao, Y. Physicochemical properties determine nanomaterial cellular uptake, transport, and fate. *Acc. Chem. Res.* **2013**, *46*, 622−631.
(12) Sharifi, S.; Behzadi, S.; Laurent, S.; Laird Forrest, M.; Stroeve, P.; Mahmoudi, M. Toxicity of nanomaterials. *Chem. Soc. Rev.* **2012**, *41*, 2323−2343.
(13) Liu, H.; Chen, D.; Li, L.; Liu, T.; Tan, L.; Wu, X.; Tang, F. Multifunctional gold nanoshells on silica nanorattles: a platform for the combination of photothermal therapy and chemotherapy with low systemic toxicity. *Angew. Chem., Int. Ed.* **2011**, *50*, 891−895.
(14) Wang, S.; Huang, P.; Nie, L.; Xing, R.; Liu, D.; Wang, Z.; Lin, J.; Chen, S.; Niu, G.; Lu, G.; Chen, X. Single continuous wave laser induced photodynamic/plasmonic photothermal therapy using photosensitizer-functionalized gold nanostars. *Adv. Mater.* **2013**, *25*, 3055−3061.
(15) Vines, J. B.; Yoon, J.-H.; Ryu, N.-E.; Lim, D.-J.; Park, H. Gold Nanoparticles for Photothermal Cancer Therapy. *Front. Chem.* **2019**, *7*, 167.
(16) Guo, L.; Panderi, I.; Yan, D. D.; Szulak, K.; Li, Y.; Chen, Y.-T.; Ma, H.; Niesen, D. B.; Seeram, N.; Ahmed, A.; Yan, B.; Pantazatos, D.; Lu, W. A comparative study of hollow copper sulfide nanoparticles and hollow gold nanospheres on degradability and toxicity. *ACS Nano* **2013**, *7*, 8780−8793.
(17) Gad, S. C.; Sharp, K. L.; Montgomery, C.; Payne, J. D.; Goodrich, G. P. Evaluation of the toxicity of intravenous delivery of auroshell particles (gold-silica nanoshells). *Int. J. Toxicol.* **2012**, *31*, 584−594.
(18) Chen, Y.; Montana, D. M.; Wei, H.; Cordero, J. M.; Schneider, M.; Le Guével, X.; Chen, O.; Bruns, O. T.; Bawendi, M. G. Shortwave Infrared in Vivo Imaging with Gold Nanoclusters. *Nano Lett.* **2017**, *17*, 6330.
(19) Zheng, K.; Setyawati, M. I.; Leong, D. T.; Xie, J. Observing antimicrobial process with traceable gold nanoclusters. *Nano Res.* **2021**, *14*, 1026−1033.
(20) Li, H.; Li, H.; Wan, A. Luminescent Gold Nanoclusters for in Vivo Tumor Imaging. *Analyst* **2020**, *145*, 348−363.
(21) Kaiyuan, Z.; Magdiel, I. S.; David, T. L.; Jianping, X. Overcoming bacterial physical defenses with molecule-like ultrasmall antimicrobial gold nanoclusters. *ACS Biomater. Sci. Eng.* **2021**, *6*, 941−950.
(22) Yeh, H.-C.; Sharma, J.; Han, J. J.; Martinez, J. S.; Werner, J. H. A DNA–silver nanocluster probe that fluoresces upon hybridization. *Nano Lett.* **2010**, *10*, 3106.
(23) Zhang, C.; Zhou, Z.; Qian, Q.; Gao, G.; Li, C.; Feng, L.; Wang, Q.; Cui, D. Glutathione-capped fluorescent gold nanoclusters for dual-modal fluorescence/X-ray computed tomography imaging. *J. Mater. Chem. B* **2013**, *1*, 5045.
(24) Zhang, X.-D.; Wu, D.; Shen, X.; Liu, P.-X.; Fan, F.-Y.; Fan, S.-J. In vivo renal clearance, biodistribution, toxicity of gold nanoclusters. *Biomaterials* **2012**, *33*, 4628−4638.
(25) Tang, S.; Peng, C.; Xu, J.; Du, B.; Wang, Q.; Vinluan, R. D.; Yu, M.; Kim, M. J.; Zheng, J. Tailoring Renal Clearance and Tumor Targeting of Ultrasmall Metal Nanoparticles with Particle Density. *Angew. Chem., Int. Ed. Engl.* **2016**, *55*, 16039−16043.
(26) Katla, S. K.; Zhang, J.; Castro, E.; Bernal, R. A.; Li, X. Atomically Precise Au25 (SG) 18 Nanoclusters: Rapid Single-Step Synthesis and Application in Photothermal Therapy. *ACS Appl Mater Interfaces* **2018**, *10*, 75−82.
(27) Huang, P.; Lin, J.; Wang, S.; Zhou, Z.; Li, Z.; Wang, Z.; Zhang, C.; Yue, X.; Niu, G.; Yang, M.; Cui, D.; Chen, X. Photosensitizer-conjugated silica-coated gold nanoclusters for fluorescence imaging-guided photodynamic therapy. *Biomaterials* **2013**, *34*, 4643−4654.
(28) Jiang, X.; Du, B.; Huang, Y.; Yu, M.; Zheng, J. Cancer Photothermal Therapy with ICG-Conjugated Gold Nanoclusters. *Bioconjugate Chem.* **2020**, *31*, 1522−1528.
(29) Zhang, X.-D.; Chen, J.; Luo, Z.; Wu, D.; Shen, X.; Song, S.-S.; Sun, Y.-M.; Liu, P.-X.; Zhao, J.; Huo, S.; Fan, S.; Fan, F.; Liang, X.-J.; Xie, J. Enhanced Tumor Accumulation of Sub-2 Nm Gold Nanoclusters for Cancer Radiation Therapy. *Adv. Healthcare Mater.* **2014**, *3*, 133−141.
(30) Hu, G.; Wang, Y.; He, Q.; Gao, H. Multistage drug delivery system based on microenvironment-responsive dendrimer-gelatin nanoparticles for deep tumor penetration. *RSC Adv.* **2015**, *5*, 85933−85937.
(31) Ruan, S.; He, Q.; Gao, H. Matrix metalloproteinase triggered size-shrinkable gelatin-gold fabricated nanoparticles for tumor microenvironment sensitive penetration and diagnosis of glioma. *Nanoscale* **2015**, *7*, 9487−9496.
(32) Zou, Z.; He, D.; He, X.; Wang, K.; Yang, X.; Qing, Z.; Zhou, Q. Natural gelatin capped mesoporous silica nanoparticles for intracellular acid-triggered drug delivery. *Langmuir* **2013**, *29*, 12804−12810.
(33) Egeblad, M.; Werb, Z. New functions for the matrix metalloproteinases in cancer progression. *Nat. Rev. Cancer* **2002**, *2*, 161−174.
(34) Xu, J.-H.; Gao, F.-P.; Liu, X.-F.; Zeng, Q.; Guo, S.-S.; Tang, Z.-Y.; Zhao, X.-Z.; Wang, H. Supramolecular gelatin nanoparticles as matrix metalloproteinase responsive cancer cell imaging probes. *Chem. Commun.* **2013**, *49*, 4462−4464.
(35) Li, L.; Fu, S.; Chen, C.; Wang, X.; Fu, C.; Wang, S.; Guo, W.; Yu, X.; Zhang, X.; Liu, Z.; Qiu, J.; Liu, H. Microenvironment-Driven Bioelimination of Magnetoplasmonic Nanoassemblies and Their Multimodal Imaging-Guided Tumor Photothermal Therapy. *ACS Nano* **2016**, *10*, 7094−7105.
(36) Wei, Y.; Zhang, J.; Zheng, Q.; Miao, J.; Alvarez, P. J.; Long, M. Quantification of photocatalytically-generated hydrogen peroxide in the presence of organic electron donors: Interference and reliability considerations. *Chemosphere* **2021**, *279*, 130556.
(37) Bahmanzadeh, S.; Ruzgas, T.; Sotres, J. Proteolytic degradation of gelatin-tannic acid multilayers. *J. Colloid Interface Sci.* **2018**, *526*, 244−252.
(38) Gonçalves, L. C.; Seabra, A. B.; Pelegrino, M. T.; de Araujo, D. R.; Bernardesc, J. S.; Haddad, P. S. Superparamagnetic iron oxide nanoparticles dispersed in Pluronic F127 hydrogel: potential uses in topical applications. *RSC Adv.* **2017**, *7*, 14496−14503.
(39) Peters, S.; Peredkov, S.; Neeb, M.; Eberhardt, W.; Al-Hada, M. Size-dependent XPS spectra of small supported Au-clusters. *Surf. Sci.* **2013**, *608*, 129−134.
(40) Sasidharan, S.; Bahadur, D.; Srivastava, R. Protein-Poly(amino acid) Nanocore-Shell Mediated Synthesis of Branched Gold Nanostructures for Computed Tomographic Imaging and Photothermal Therapy of Cancer. *ACS Appl. Mater. Interfaces* **2016**, *8*, 15889−15903.
(41) Mo, R.; Gu, Z. Tumor microenvironment and intracellular signal-activated nanomaterials for anticancer drug delivery. *Mater. Today* **2016**, *19*, 274−283.
(42) Reddy, A. S.; Wozniak, D. F.; Farber, N. B.; Dearborn, J. T.; Fowler, S. C.; Sands, M. S. Bone Marrow Transplantation Alters the

https://doi.org/10.1021/acsomega.1c07324
ACS Omega 2022, 7, 8928−8937

Tremor Phenotype in the Murine Model of Globoid-Cell Leukodystrophy. *J. Clin. Med.* **2012**, *1*, 1−14.
(43) Nomura, S.; Morimoto, Y.; Tsujimoto, H.; Arake, M.; Harada, M.; Saitoh, D.; Hara, I.; Ozeki, E.; Satoh, A.; Takayama, E.; Hase, K.; Kishi, Y.; Ueno, H. Highly reliable, targeted photothermal cancer therapy combined with thermal dosimetry using a near-infrared absorbent. *Sci. Rep.* **2020**, *10*, 9765.
(44) Liu, X.; Zhang, X.; Zhu, M.; Lin, G.; Liu, J.; Zhou, Z.; Tian, X.; Pan, Y. PEGylated Au@Pt Nanodendrites as Novel Theranostic Agents for Computed Tomography Imaging and Photothermal/Radiation Synergistic Therapy. *ACS Appl. Mater. Interfaces* **2017**, *9*, 279−285.
(45) Yong, Y.; Cheng, X.; Bao, T.; Zu, M.; Yan, L.; Yin, W.; Ge, C.; Wang, D.; Gu, Z.; Zhao, Y. Tungsten Sulfide Quantum Dots as Multifunctional Nanotheranostics for In Vivo Dual-Modal Image-Guided Photothermal/Radiotherapy Synergistic Therapy. *ACS Nano* **2015**, *9*, 12451−12463.
(46) Xiao, Q.; Zheng, X.; Bu, W.; Ge, W.; Zhang, S.; Chen, F.; Xing, H.; Ren, Q.; Fan, W.; Zhao, K.; Hua, Y.; Shi, J. A core/satellite multifunctional nanotheranostic for in vivo imaging and tumor eradication by radiation/photothermal synergistic therapy. *J. Am. Chem. Soc.* **2013**, *135*, 13041−13048.
(47) Gao, L.; Zhuang, J.; Nie, L.; Zhang, J.; Zhang, Y.; Gu, N.; Wang, T.; Feng, J.; Yang, D.; Perrett, S.; Yan, X. Intrinsic peroxidase-like activity of ferromagnetic nanoparticles. *Nat. Nanotechnol.* **2007**, *2*, 577−583.
(48) Sang-Mook, Y.; Jin-Sung, P.; Ke, L.; Ki-Baek, J.; Hazzel, J.A.; Young-Rok, K. Modulation of the peroxidase-like activity of iron oxide nanoparticles by surface functionalization with polysaccharides and its application for the detection of glutathione. *Carb. Pol.* **2021**, *267*, 118164.
(49) Daneshvar, F.; Salehi, F.; Karimi, M.; Vais, R. D.; Mosleh-Shirazi, M. A.; Sattarahmady, N. Combined X-ray radiotherapy and laser photothermal therapy of melanoma cancer cells using dual-sensitization of platinum nanoparticles. *J Photochem Photobiol B* **2020**, *203*, 111737.
(50) Sun, Q.; Wu, J.; Jin, L.; Hong, L.; Wang, F.; Mao, Z.; Wu, M. Cancer cell membrane-coated gold nanorods for photothermal therapy and radiotherapy on oral squamous cancer. *J Mater Chem B.* **2020**, *8*, 7253−7263.
(51) Jeon, M.; Halbert, M. V.; Stephen, Z. R.; Zhang, M. Iron Oxide Nanoparticles as T_1 Contrast Agents for Magnetic Resonance Imaging: Fundamentals, Challenges, Applications, and Prospectives. *Adv. Mater.* **2021**, *33*, 1906539.
(52) Wei, H.; Wiśniowska, A.; Fan, J.; Harvey, P.; Li, Y.; Wu, V.; Hansen, E. C.; Zhang, J.; Kaul, M. G.; Frey, A. M.; Adam, G.; Frenkel, A. I.; Bawendi, M. G.; Jasanoff, A. Single-nanometer iron oxide nanoparticles as tissue-permeable MRI contrast agents. *Proc. Natl. Acad. Sci. U.S.A.* **2021**, *118*, 2102340118.
(53) Bogdanov, A. A., Jr.; Dixon, A. J.; Gupta, S.; Zhang, L.; Zheng, S.; Shazeeb, M. S.; Zhang, S.; Klibanov, A. L. Synthesis and Testing of Modular Dual-Modality Nanoparticles for Magnetic Resonance and Multispectral Photoacoustic Imaging. *ACS Bioconjug. Chem.* **2016**, *27*, 383−390.
(54) Liu, J.; Wang, D.; Wang, G. Magnetic-gold theranostic nanoagent used for targeting quad modalities T_1 & T_2-MRI/CT/PA imaging and photothermal therapy of tumours. *RSC Adv.* **2021**, *11*, 18440−18447.

https://doi.org/10.1021/acsomega.1c07324
ACS Omega 2022, 7, 8928−8937